PERFORMANCE OF TIMBER BOARD MODELS FOR PREDICTION OF LOCAL BENDING STIFFNESS AND STRENGTH—WITH APPLICATION ON DOUGLAS FIR SAWN TIMBER

*A. Olsson**

Professor
Department of Building Technology
Linnaeus University
Växjö, Sweden
E-mail: anders.olsson@lnu.se

G. Pot

Associate Professor
Arts et Métiers Sciences et Technologies
LABOMAP Université Bourgogne Franche-Comté
HESAM Université, F-71250
Cluny, France
E-mail: guillaume.pot@ensam.eu

J. Viguier

Associate Professor
Arts et Métiers Sciences et Technologies
LABOMAP, Université Bourgogne Franche-Comté
HESAM Université, F-71250
Cluny, France
E-mail: joffrey.viguier@ensam.eu

M. Hu

Assistant Professor
Department of Building Technology
Linnaeus University
Växjö, Sweden
E-mail: min.hu@lnu.se

J. Oscarsson

Associate Professor
Department of Building Technology
Linnaeus University
Växjö, Sweden
E-mail: jan.oscarsson@lnu.se

Abstract. Efficient utilization of structural timber requires accurate methods for machine strength grading. One of the most accurate methods presented this far is based on data of local fiber orientation on board surfaces, obtained from laser scanning. In this paper, two potential improvements of this method are examined. The first one consists of replacing a model based on simple integration over cross sections of boards for calculation of local bending stiffness by a 3D solid finite element (FE) model from which local bending stiffness is derived. The second improvement concerns replacement of a simple model for the fiber orientation in the interior of board by a more advanced one taking location of pith and growth direction of knots

* Corresponding author

into account. Application of the alternative models on a sample of more than 200 Douglas fir boards, size 40 mm × 100 mm × 3000 mm, cut from large logs, show that each of the evaluated model improvements contributes to improved grading accuracy. When local bending stiffness is calculated utilizing the herein suggested FE model in combination with the improved model of fiber orientation in the interior of boards, a coefficient of determination to bending strength as high as 0.76 is obtained. For comparison, a coefficient of determination of 0.71 is obtain using the simpler original models.

Keywords: Dynamic excitation, lumber, modulus of elasticity, modulus of rupture, stress grading, tracheid effect.

INTRODUCTION

Strength and stiffness of timber vary substantially between pieces and therefore effective utilization of structural timber requires machine strength grading, using indicating properties (IPs), and machines by which strength could be predicted with a certain level of accuracy. In many of the methods and machines used on the market today, especially in Europe, the longitudinal dynamic modulus of elasticity (MoE) is utilized as an IP to edgewise bending or tensile strength (Oscarsson 2014). The vibration signal from dynamic excitation, the weight or the density, and the dimensions of the board can be measured fast and accurately with machines that are comparatively inexpensive, and the dynamic MoE, representing an average MoE of the board, is calculated using a simple equation. However, the relationship between longitudinal dynamic MoE and strength is rather weak. For Norway spruce (*Picea abies*) the coefficient of determination, R^2, between longitudinal dynamic MoE and edgewise bending strength is often about 0.5 or slightly higher when linear regression is applied (Hanhijärvi and Ranta-Maunus 2008; Olsson and Oscarsson 2017) and differs between different samples and investigations. For Douglas fir, the coefficient of determination between dynamic MoE and bending strength is often lower than for spruce. Olsson et al (2018a) reported an R^2 of 0.47 for a sample of more than 800 structural sized Douglas fir timber boards of mixed dimensions.

There are grading machines on the market in which high-resolution X-ray scanning is combined with dynamic MoE. This combination of techniques represents the most accurate strength grading method of those common on the market today (Briggert et al 2020). The information added by X-ray scanning concerns the variation of density within a board which means that knot measures can be derived and used in definitions of IPs. In an extensive study performed by Hanhijärvi and Ranta-Maunus (2008), comprising more than 1000 boards of Norway spruce and 1000 boards of Scots pine (*Pinus sylvestris*), assessments of various strength grading machines and of the relationship between IPs and strength in both tension and bending were performed. The method/IP that showed the best performance, with respect to coefficient of determination between IP and bending or tensile strength, was based on a combination of data from dynamic excitation and X-ray scanning. For Norway spruce timber, loaded to failure in bending, this method/IP gave an R^2 to bending strength of 0.64. When dynamic MoE (also assessed by equipment from the same company) was calculated on the basis of resonance frequency and board density, and on resonance frequency alone, R^2 of 0.57 and 0.48, respectively, were achieved for the same timber. For the sample of Scots pine, the improvement in grading accuracy when using the method/IP based on the combination of X-ray scanning and dynamic MoE, rather than on dynamic MoE alone, was larger than what it was for the sample of Norway spruce. Other studies that give examples of the performance of the same or similar equipment are Bacher (2008) and Nocetti et al (2010).

Olsson et al (2013) suggested a strength grading method based on dot laser scanning and utilization of the tracheid effect (Matthews and Beech 1976; Soest et al 1993; Briggert et al 2018), which gives high-resolution information of the fiber orientation on board surfaces, and knowledge of dynamic MoE. Based on knowledge of local fiber orientation, wood material stiffness properties in

orthogonal directions, and calculation of board stiffness on the cross-sectional level using a rather simple integration model, an IP defined as the lowest local edgewise bending MoE found along a board was established. Comprehensive investigations on a large sample of Norway spruce boards of mixed dimensions (Olsson and Oscarsson 2017) and on samples of Norway spruce, Douglas fir, and European oak, respectively (Olsson et al 2018a), showed that application of this method gives accurate predictions of bending strength and high yields in high strength classes. For example, coefficients of determination to bending strength of about 0.68-0.70 was achieved for Norway spruce. For Douglas fir, the method has up until now only been evaluated for one sample, consisting of about 800 boards of three different dimensions (Olsson et al 2018a), which gave a coefficient of determination to bending strength of 0.62 (compared with 0.47 using dynamic MoE as IP). Furthermore, this method has also been used for prediction of tensile strength of glulam lamellas. In a study by Briggert et al (2020) on a sample of more than 900 Norway spruce boards of mixed dimensions, a coefficient of determination to tensile strength of 0.66 (using linear regression) and 0.70 (using nonlinear regression) was obtained. For the same sample, a coefficient of determination of 0.46 (linear regression) was obtained using dynamic MoE as IP to tensile strength. Briggert et al (2020) also showed that the method based on fiber orientation detected on surfaces gives almost as accurate prediction of strength when applied on Norway spruce boards with sawn surfaces as when applied on boards with planed surfaces. So far, no other method that gives more accurate predictions of strength when assessed on large samples of sawn timber, ie samples large enough to give basis for settings for a machine controlled strength grading method (EN 14081-2 2018), seems to exist. However, there is potential for improvements of the method. This was shown by Hu et al (2018) who suggested 1) a new way to estimate the fiber direction in the interior of a board by utilizing knowledge of location of pith in relation to the board cross section and 2) use of a 3D finite element (FE) model, rather than simple integration over the cross section, to calculate local bending stiffness. In Hu et al (2018), local bending stiffness was calculated on the basis of fiber direction data from laser scanning of two Norway spruce boards, using the original as well as improved versions of the method/model, and the results were compared with local bending stiffness calculated on the basis of local strains, obtained from digital image correlation (DIC) of the boards when they were subjected to constant bending moment. Comparisons for the two boards included in that study showed that suggested improvements of the model lead to substantial improvement regarding resemblance between bending stiffness profiles obtained based on the model and of DIC, respectively.

Regarding location of pith, new methods to determine this have been developed in the last few years. Habite et al (2020) presented a method to automatically determine location of pith in relation to board cross sections, based on optical scanning of the four longitudinal surfaces of boards and identification of annular ring pattern on images of the surfaces. Faster and more robust methods, based on optical scanning of longitudinal board surfaces in combination with machine learning, were developed by Habite et al (2021) and in particular Habite et al (2022). Thus, it is possible to determine pith location in production speed at sawmills and to utilize this in models of boards.

The objective of the present study is to investigate if the improvements of the method/model, suggested by Hu et al (2018), give more accurate predictions of strength than what the original versions of the method (Olsson et al 2013; Olsson and Oscarsson 2017; Olsson et al 2018a) does, by applying this method on a database of 241 Douglas fir boards.

Before proceeding with the present study, some other recent research works, also aiming at improved modeling and strength grading on sawn timber by utilizing the possibilities of modern scanning techniques and/or FE analyses should be mentioned, namely the following.

- Viguier et al (2017) suggested a grading method based on a combination of data from

tracheid effect scanning and X-ray scanning. In this method, data of local fiber orientation was utilized in a similar way as by Olsson et al (2013) but using the data from the two wide faces only. Furthermore, local density was used to assess local material properties. An elaborate calculation scheme, including assessment of local stresses corresponding to edgewise bending of the board, was used to predict board strength. The method was successfully applied on large samples of Norway spruce and Douglas fir boards and the grading accuracy obtained was similar to the one obtained by Olsson et al (2013) and Olsson and Oscarsson (2017).

- Lukacevic et al (2015) developed a procedure to reconstruct location of pith and 3D knot geometry on the basis of data from traditional, 2D X-ray scanning. The authors used the determined 3D knot geometry as basis for different IPs to bending strength and very high coefficients of determination to strength were obtained, when combining up to seven different predictor variable in linear regression, but the sample size used was too small to prove that the models were reliable. Later the same research group has presented improved models for 3D reconstruction of knots (Kandler et al 2016) and for fiber orientation in the surroundings of knots (Lukacevic et al 2019) on the basis of data from tracheid effect scanning combined with a mathematical model for fiber orientation in 3D around knots developed by Foley (2003).
- Sarnaghi and van de Kuilen (2019) identified size and location of knots manually/visually and established based on such data 3D models of knots and, utilizing a grain flow analogy, local fiber orientation of 102 boards of Norway spruce and 150 boards of Douglas fir. The fiber orientation models in turn gave basis for FE models by which local stresses corresponding to tensile loading of boards were calculated. By performing nonlinear regression utilizing two different stress concentration factors (which were calculated on the basis of stresses from FE simulation) in combination with knowledge of axial dynamic MoE (in total utilizing five predictor variables in the regression model) coefficients of determination to tensile strength of up to 0.75 and 0.72 were obtained for the samples of Norway spruce and Douglas fir, respectively.
- Jenkel and Kaliske (2018) presented an advanced FE model of timber boards including plasticity and fracture mechanics for prediction of tensile strength. Knot geometry and local fiber orientation were determined in a similar way as by Sarnaghi and van de Kuilen (2019). The material and mechanical model suggested may be the most advance one this far used to predict tensile strength of sawn timber but the assumptions made regarding material properties were, in comparison, simple and based on limited experimental data. Regarding comparison of calculated and experimentally determined tensile strength of boards, results were presented only for selected boards and not for a full sample. Thus, coefficients of determination to strength comparable to those obtained from other investigations/methods were not presented.
- As an example of recent work in this field carried out by a non-European research group, Wright et al (2019) automatically identified knots on surfaces of 171 pieces of loblolly pine lumber and based on this evaluated different knot measures for prediction of bending strength of boards.

In summary, several rather similar attempts to develop accurate methods for machine strength grading by utilizing high-resolution data and/or models of boards, including knot geometry and local fiber orientation, have been made in recent years. Further work in this area should consist of systematic and critical assessment of potential improvements regarding—representation of knot geometry and fiber orientation within boards; mechanical, material, and numerical models employed; definitions of IPs—such that the most critical limitations of the methods presented this far are successively identified and eliminated. As explained above, the aim of the present paper is to contribute in this respect.

MATERIAL AND DATA FROM INTRODUCTORY INVESTIGATIONS

Eight logs of Douglas fir (*Pseudotsuga menziesii* [Mirb.] Franco), cultivated in France, were originally selected to investigate structural properties of sawn Douglas fir timber as functions of the distance to pith, and to investigate the accuracy of different methods for machine strength grading when applied on boards from different parts of logs. Therefore, logs with large diameters of about 50 cm were selected. From each such log a large number of boards were cut, including a significant number from outerwood. Herein outerwood boards are defined as boards that are located, at least partly, outside a radius of 200 mm from the pith. From the eight logs, 241 boards (between 24 and 36 boards from each log) of nominal dimensions 40 mm × 100 mm × 3000 mm and without significant wane were sawn and dried in an industrial sawmill. Before sawing, a pattern was painted on the butt-end of each log such that the position of each board could be related to the log cross section also after sawing. In Fig 1, the butt end of log no. 7, and the pattern painted on it, is shown. Indicated in the figure are also the reconstructed position of each of the boards cut from the log, and two coordinate systems used to define coordinates of the entire log cross section and of a single board cross section, respectively. Such coordinate systems were used to determine the position and orientation of each board in relation to the pith of the log. Thus, the material used for the present investigation comprise 241 Douglas fir boards for which position and orientation in relation to the pith of the log are known. The accuracy/error of location of pith should be within a couple of millimeters up to about one centimeter in the butt-end of the boards and up to a few centimeters in the top end of the boards. Since log top-ends were not painted, the accuracy of location of pith was lower in the top-end than in the butt-end.

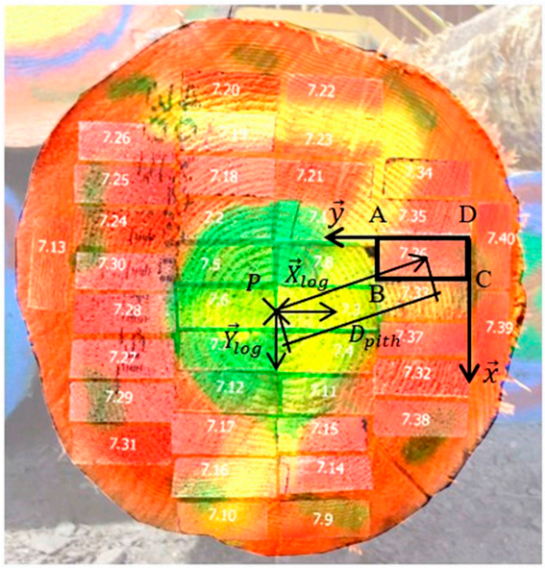

Figure 1. Photomontage of the painted butt-end of one log (no. 7, as an example) with the cross section of the 40 mm × 100 mm sawn boards superposed on it. The 15 annual rings closest to the pith are painted in a different color to enable localization of juvenile wood of the boards cut from the log. For board no. 7.36, framed in black, a local coordinate system (D, $\vec{x}$, $\vec{y}$, $\vec{z}$) is indicated. D_{pith} mark the distance between pith and the center of the board cross section. Points A, B, C, and D represent the positions of the four corners of the cross section.

METHODS

Collection of Data and Definitions of Properties

Below it is described how the data from the introductory investigation, in combination with additional measurements, give basis for and are utilized in models and definitions of IPs, and to determine properties like local static MoE and bending strength.

Scanning to obtain fiber orientation, color images, and local density. A CombiScan+ industrial scanner from the company LuxScan Technologies (Weinig group) was used to measure board dimensions, to take red-green-blue (RGB) images of surfaces, to determine local fiber orientation on surfaces and to determine local density of the boards, when the boards are fed longitudinally through the scanner. Local fiber orientation on surfaces was obtained by means of dot lasers and utilization of the tracheid effect, giving a resolution of determined in-plane fiber direction in longitudinal and transversal direction of the

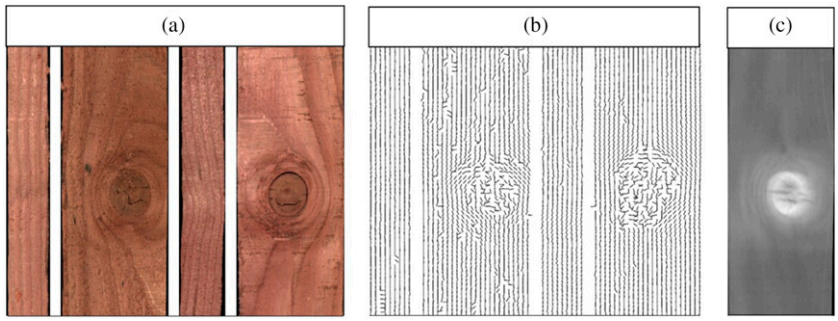

Figure 2. Data obtained using the scanner, displayed for a 250 mm long section of a board; (a) RGB images of four sides of the board, (b) determined in-plane fiber directions on four sides (resolution in longitudinal direction reduced to 4 mm in the images), and (c) determined local density, averaged over the thickness direction, where bright areas represent high density and dark areas represent low density.

board of about 1 mm and 4 mm, respectively, on all four sides of the board. Local density, determined as an average value over the thickness direction of a board, was obtained by means of X-ray giving a resolution in longitudinal and transversal board direction of about 1 mm and 0.3 mm, respectively. However, data of density obtained from X-ray scanning was not utilized in the present investigation. Instead, the density was determined manually, see "Determination of density, moisture content and resonance frequency" section. In Fig 2, examples of data obtained using the scanner is displayed showing, for a 250 mm long section of a board, 1) RGB images of four sides, 2) determined in-plane fiber directions on four sides (resolution in longitudinal direction reduced to 4 mm in the images), and 3) determined local density where bright areas represent high density. Fibers within round knots are almost parallel with the direction of the branch/knot itself, ie the fiber direction is close to perpendicular to the wide faces of the board surfaces displayed. Laser dots illuminating surfaces of round knots become almost circular in shape and the determined in-plane fiber directions become, within the knot areas, more or less randomly oriented. In the surroundings of the knots, in-plane fiber directions resemble flow lines around the knots. Some of the detected local fiber directions, also in clear wood parts of the surfaces, diverge, seemingly randomly, from the longitudinal direction of the board (Fig 2[b]). This is due to the roughness of the sawn wood surfaces, as discussed by Daval et al (2015) and Briggert et al (2020).

Determination of density, MC, and resonance frequency. For each board, the board mass (m), the board length (L), depth (h), and thickness (t) and the board MC (u_s) were determined manually. A scale was used for weighing, and a Gann HT 95 pin-type moisture meter was used to determine the MC. To determine the lowest longitudinal resonance frequency of the board, (f_1), an E-scan machine from LuxScan Technologies was employed.

On the basis of these data the *average board density*, adjusted to 12% MC (MC), was calculated as

$$\rho_{\mathrm{corr}} = \frac{m}{L \cdot h \cdot t}\left(1 - \frac{u_s - 12}{200}\right). \qquad (1)$$

Furthermore, the *dynamic axial MoE*, adjusted with respect to MC, was calculated as

$$E_{\mathrm{a,corr}} = 4\frac{m}{L \cdot h \cdot t} f_1^2 L^2 \left(1 + \frac{u_s - 12}{100}\right). \qquad (2)$$

The adjustments with respect to MC were done in accordance with the European standard (EN 384 2016).

Destructive Tests and Determination of Local Bending MoE and Bending Stiffness

In Fig 3, the test arrangement for a four-point bending test according to the European standard

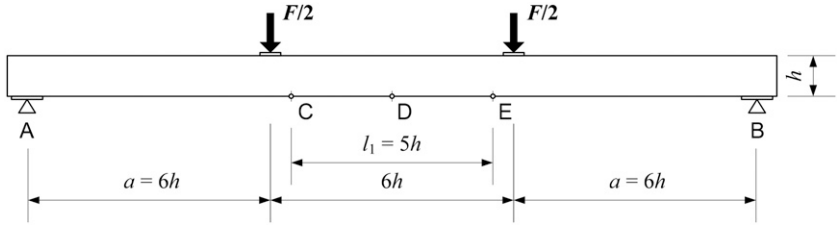

Figure 3. Test setup for determination of local MoE and bending strength in edgewise bending.

(EN 408 2010) is displayed. Based on such a test the local static MoE in bending, adjusted to 12% MC, was determined as

$$E_{m,l} = \frac{a l_1^2 (F_2 - F_1)}{16 I (w_2 - w_1)} \quad (3)$$

where a is the distance between one of the point loads and the closest support, F is the total loading (two load levels, F_1 and F_2, respectively), $l_1 = 5h$ is the span for determination of local MoE, I the second moment of inertia ($th^3/12$) and w the center deflection of the span l_1 (D in relation to C and E, see Fig 3).

When $E_{m,l}$ has been determined in accordance with Eq 3 a correction with respect to MC was performed as

$$E_{m,l,corr} = E_{m,l}\left(1 + \frac{u_s - 12}{100}\right). \quad (4)$$

The bending strength f_m was calculated in accordance with EN 408 as

$$f_m = \frac{3 F_{max}\, a}{b h^2} \quad (5)$$

where F_{max} is the maximum value of the total load applied by the two point loads. This bending strength is then corrected for boards with a depth less than 150 mm, ie the size effect is taken into account, according to the European standard EN 384, clause 5.4.3 as

$$f_{m,h} = \frac{f_m}{k_h} \quad (6)$$

where

$$k_h = \min \begin{cases} \left(\frac{150}{h}\right)^{0.2} \\ 1.3 \end{cases}. \quad (7)$$

In this research, only pieces that broke within the maximum/constant bending zone, ie within the point loads, was considered. Thus, all the boards that broke *outside* the point loads, which was the case for 20 boards, were disregarded for further evaluation which means that $241 - 20 = 221$ boards are considered in the following evaluation.

Models for Calculation of Local Bending Stiffness

Below a summary of the grading method suggested by Olsson et al (2013) is given, followed by descriptions of the improvements of the method suggested by Hu et al (2018).

Stiffness based on integration over cross section. The machine strength grading method (Olsson et al 2013) which is the basis for the present investigation can, in brief, be divided into three steps below:

1. It is assumed that the in-plane fiber direction, represented by an angle, φ, detected locally on a board surface (see Fig 4[a]) is representative for a small area (a few square millimeters, depending on resolution of data of fiber direction) of the surface. Furthermore, the fiber orientation in the interior of the board is a function of the fiber orientation on the surfaces. The original way to determine the fiber orientation in the interior of the board was that φ is applied to a certain depth into the board, ie φ is assumed to be valid for the sub volume $\Delta x \Delta A$, as illustrated in Fig 4(a) and (b).
2. Values of nine independent material parameters of the wood material (MoEs, shear moduli and Poisson's ratios) are adopted. Values for Douglas fir used in the present study are

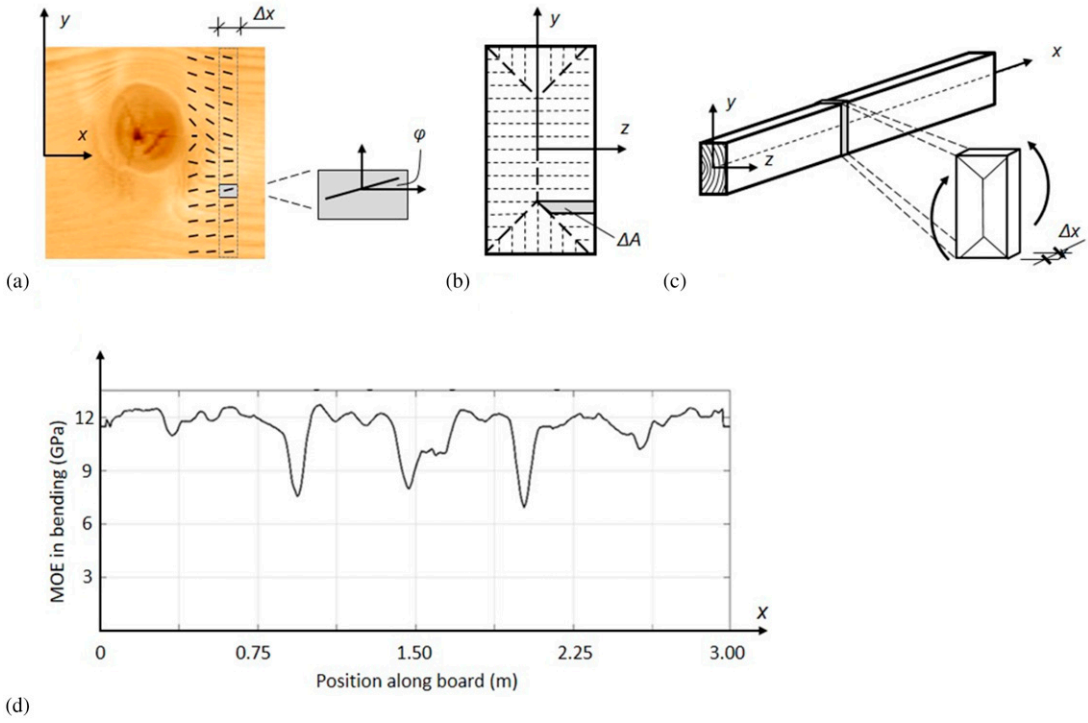

Figure 4. (a) Local in-plane fiber directions identified on a member's surface, (b) cross section divided into subareas implying that the exhibited angle φ and corresponding MoE in the longitudinal direction, $E_x(x, y, z)$, is valid within the volume $\Delta A \Delta x$, (c) segment of length Δx for which the edgewise bending MoE is calculated by stiffness integration over the segment's cross section, and (d) a bending MoE profile, each value along the graph representing the average edgewise bending MoE of the surrounding 90 mm.

identical to those used in Olsson et al (2018a). On the basis of these, and the local fiber direction, the corresponding local MoE, $E_x(x, y, z)$, valid in longitudinal direction x, is calculated by transformation for every position within the volume of the board.

3. The cross-sectional edgewise bending stiffness, for positions x (in steps of Δx) along the board, is calculated by numerical integration over the cross section (see Fig 4[c]) as

$$EI_z(x) = \sum_A E_x (y - \bar{y})^2 \Delta A \qquad (8)$$

where

$$\bar{y} = \frac{\sum_A E_x y \Delta A}{\sum_A E_x \Delta A} \qquad (9)$$

and y is the coordinate in depth direction of the center point of each small subarea ΔA of the cross-sectional area A. Eqs 8 and 9 enable calculation of an edgewise bending MoE, as function of the position along the board, as

$$E_b(x) = \frac{12 EI_z(x)}{th^3} \qquad (10)$$

where t and h are the thickness and depth, respectively, of the board cross sections.

In Fig 4(d), a calculated MoE profile, established by calculating a moving average of $E_b(x)$ over a length of 90 mm is displayed. IPs to bending strength, established on the basis of the lowest value of such MoE-profiles in combination with axial dynamic MoE were evaluated in eg Olsson et al (2013), Olsson and Oscarsson (2017), and Olsson et al (2018a). In the following the method to calculate

bending MoE as described above is referred to as the integration over cross section (IOCS) method.

Finally, two deficiencies of the described method should be pointed out. First, calculation of bending stiffness by integration of stiffness over single cross sections (of very short length, Δx) at a time, before calculating a mean stiffness over a longer distance (eg 90 mm) means that the local bending stiffness is overestimated. In reality, a short segment along the board containing for example two knots at different position in x- and y-direction may have considerably more compliance to bending than what is captured using the IOCS model. Second, the assumptions that fibers are located in the plane of each scanned surface and that the determined fiber angle at the surface is valid to a certain depth into the board, without consideration of the direction of knots within the board, do not reflect the real fiber direction within the board.

Stiffness based on FE method and simulation of bending. As an alternative to the IOCS method, Hu et al (2018) used a 3D FE model and simulation of pure bending to calculate local bending MoE. The FE model consisted of 8-node linear brick, full integration elements. The element size used was 5 mm × 5 mm × 5 mm and a convergence study indicated that this element mesh was sufficient for the present purpose. The basis for material directions locally in the board volume and the material parameters applied were the same as those defined for the IOCS method. Thus, steps (a and b) as described in the "Stiffness based on integration over cross section" section were performed before FE modeling and simulation of constant bending of the part of the board of length $l_1 = 5h$ between the two point loads.

Applying a constant bending moment, M_z, gave calculated engineering strains with a resolution corresponding to the element mesh. However, since the material direction locally depended on the fiber orientation determined based on a single laser dot the calculated strain field contained noise. Therefore, to reduce this noise, the strain in longitudinal direction in a certain element was replaced by the average strain of the surrounding area of about 20 mm × 20 mm in the xy-plane. This filtered strain field is denoted $\boldsymbol{\varepsilon}_x(x, y, z)$. In the next step, a desired longitudinal resolution of calculated bending stiffness of the board, represented by a longitudinal distance L_r (eg 50 mm), was determined. The average longitudinal strains, $\boldsymbol{\varepsilon}_{x,r}(x_p, y, z)$, over the surrounding distance, L_r, was calculated (on the basis of $\boldsymbol{\varepsilon}_x(x, y, z)$) for positions x_p, ie longitudinal strains were calculated at every nodal position of the 5 mm mesh/grid of the cross section. Note that the distance between x_p and x_{p+1} is also 5 mm due to the chosen element grid. In clear wood sections, $\boldsymbol{\varepsilon}_{x,r}(x_p, y, z)$ is close to a linear function of y, and almost independent of z, but this is not the case in sections containing knots. $\boldsymbol{\varepsilon}_{x,r}(x_p, y, z_c)$, where z_c is a selected constant position on the z-axis, was however approximated with a linear function of y, $\bar{\varepsilon}_{x,r}(x_p, y, z_c)$, determined by linear regression performed on $\boldsymbol{\varepsilon}_{x,r}(x_p, y, z_c)$.

The cross-sectional bending stiffness of the board was finally determined based on $\bar{\varepsilon}_{x,r}(x_p, y, z_c)$, ie for a given plane of $z = z_c$, at every position x_p along the board, the cross-sectional bending stiffness was calculated as

$$EI_{z,r,c}(x_p, z_c) = \frac{M_z}{\bar{\varepsilon}_{x,r}(x_p, y_1, z_c)}(y_0 - y_1) \qquad (11)$$

where y_0 is the position on the y-axis where $\bar{\varepsilon}_{x,r}(x_p, y_0, z_c) = 0$ and y_1 is any other position along the y-axis. Thus, $EI_{z,r,c}(x_p, z_c)$ is the calculated edgewise bending stiffness, of longitudinal resolution L_r, calculated based on strains in the xy-plane where $z = z_c$. Finally, the corresponding bending MoE, $E_{b,FE}(x, z_c)$, was calculated as

$$E_{b,FE}(x, z_c) = \frac{12EI_{z,r,c}(x)}{th^3}. \qquad (12)$$

Figure 5(a) shows a calculated strain field $\boldsymbol{\varepsilon}_x(x, y, z_c)$ for $z_c = h/2$, ie the strains in longitudinal direction on one wide surface of a 600 mm long part ($6h$) of a board. Thus, the strains displayed represent average strains over surrounding areas of 20 mm × 20 mm. The inclined straight lines plotted on top of the strain plot represent $\bar{\varepsilon}_{x,r}(x_p, y_1, z_c = h/2)$, ie lines of linear regression calculated on the basis of longitudinal strains calculated across vertical sections. The distance between two adjacent lines was 5 mm, determined by the size of

the element mesh. However, the strains on which these lines are based were average strains over a distance of 50 mm, ie L_r was 50 mm. In Fig 5(b) and (c), black and red dots represent calculated average strains over the distance L_r and solid lines are lines of regression calculated based on the strains for two vertical sections of the board, one free of knots (black line in Fig 5[a] and [b]) and the other with knots (red line Fig 5[a] and [c]). In the knot free section, the black dots follow the straight line very well, with a coefficient of determination $R^2 = 0.999$, whereas in the knotty section the strain values clearly deviate from the line of regression resulting in a coefficient of determination of $R^2 = 0.915$. Figure 5(d) shows the bending MoE variation in the exhibited part of the specimen, determined for the plane $z = z_c$ based on all the lines of linear regression shown in Fig 5(a).

As explained, $E_{b,FE}(x, z_z)$ can be calculated for any value of z_c from -20 mm to 20 mm (corresponding to the full board's smaller dimension). Herein a local bending MoE of resolution L_r, representing an average over the smaller dimension of the board, is calculated as

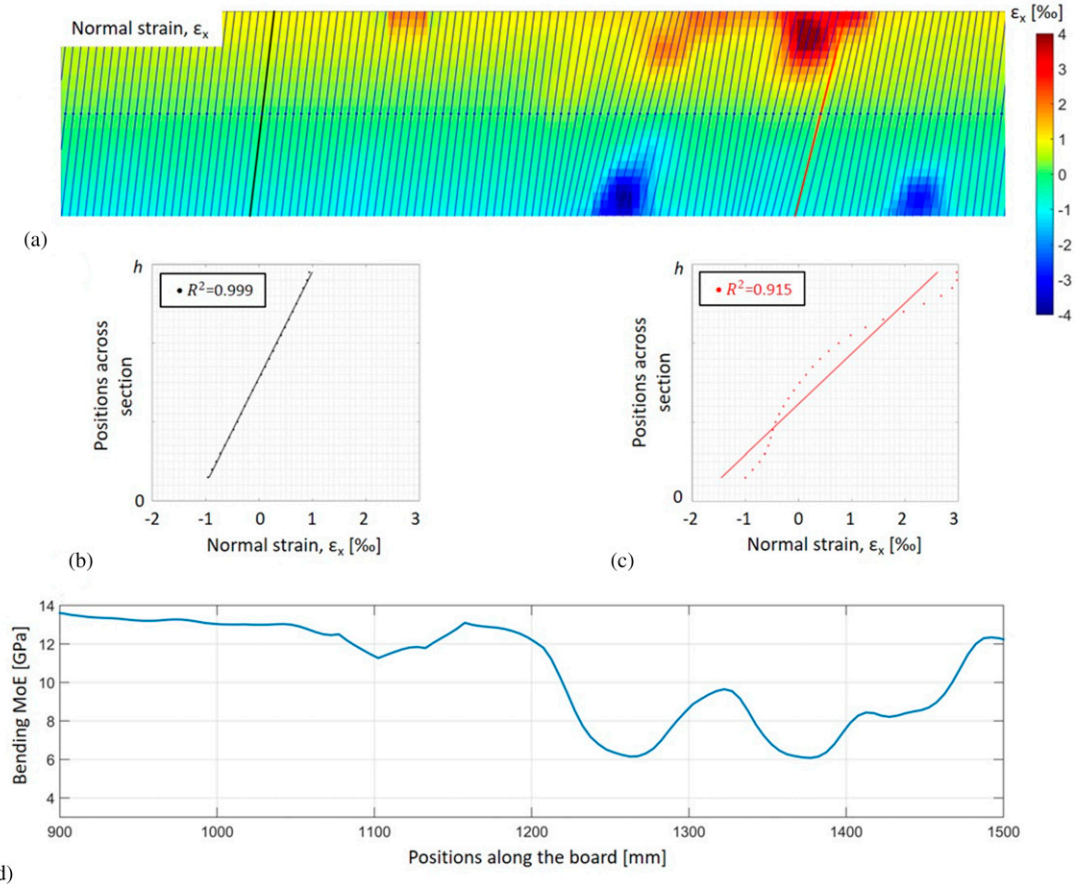

Figure 5. (a) Examples of strain distribution for a plane of $z_c = h/2$ and calculated using the FE model, where each strain value displayed represents a mean value of the surrounding area about 20 mm × 20 mm. Lines of regression of longitudinal strains across vertical cross sections are drawn on top of the strain plot. Two lines are highlighted in black and red. These are also shown in (b) and (c), respectively, along with the original strain values on which they are based. The corresponding R^2-values indicate to what extent the strains along a vertical line at a certain coordinate $z = z_c$ comply with the straight lines. (d) Bending MoE profile based on the regression lines in (a).

$$E_{\bar{b},\mathrm{FE}}(x)=\frac{1}{4}\sum_{z_c=-20;\,-5;\,5;\,20} E_{\mathrm{b,FE}}(x,z_c). \quad (13)$$

Alternative Models for Fiber Direction within Boards

In the description of the IOCS method in the "Stiffness based on integration over cross section" section, it was assumed (step a) that an in-plane fiber angle, φ, detected locally on a board surface is representative for a small area of the surface (highlighted grey area shown in Fig 4[a]) and that the fiber orientation in the interior of the board is a function of the fiber orientation on the surfaces. The original way to determine the fiber orientation in the interior of the board (Olsson et al 2013) was that φ is applied to a certain depth into the board, ie assumed valid for the sub volume $\Delta x \Delta A$ (see Fig 4[a] and [b]). This way, information from scanning of all four sides of the board is utilized but the location of the pith is not taken into account. However, location of pith determines orientation of knots, which in turn are crucial for the fiber orientation within the board. Hu et al (2018) therefore suggested an alternative model for modeling fiber orientation in the interior of boards taking location of pith into account.

Illustrations of the two alternative models for the fiber direction in the interior of the board are given in Fig 6 in which Fig 6(a) represents the original fiber angle model suggested by Olsson et al (2013), in the following referred to as fiber angle model 1 (FAM1). In this model, the fiber angle determined at a position on a board surface (red dots in Fig 6[a]) is used to represent the fiber angle in every position (shaded volume in Fig 6[a]) from the surface to a certain depth into the board (black dots in Fig 6[a]). The other model, which takes location of pith into account, is in the following referred to as fiber angle model 2 (FAM2). In this model the fiber angle in a position within the board (black dot in Fig 6[b]) is determined by the fiber angles on board surfaces at positions (red dots in Fig 6[b]) where the surfaces intersect with a straight line drawn from the pith (green dot in Fig 6[b]) through the position (black dot in Fig 6[b]) where the fiber angle shall be determined. The line intersects with two positions on board surfaces (red dots in Fig 6[b]) and the fiber angle in the position within the board (black dot in Fig 6[b]) is determined by linear interpolation of the fiber angles at the points of surface intersection. In the special case when the pith is located inside the board, the fiber direction identified in a position on the surface is used for wood between this position on the surface and the pith inside the board (constant value for all positions in the radial direction). Thus, the angle between longitudinal direction of the board and the local fibers was determined according to FAM1 and FAM2, respectively, for a set of positions, ie a 3D grid of the board volume.

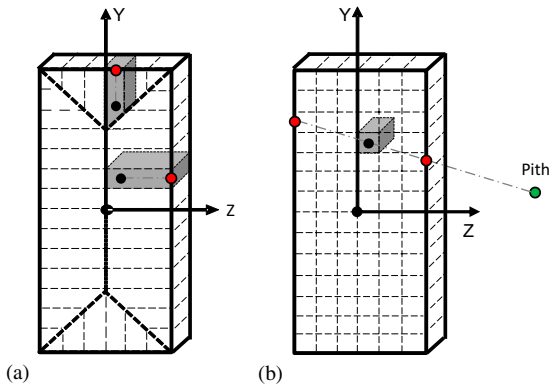

Figure 6. Models for representation, in the interior of the board, of the angle between the fiber direction and the longitudinal board direction on the basis of known such angles on the board surfaces; (a) illustration of FAM1 and (b) illustration of FAM2.

For both models the assumption is made that the longitudinal-tangential plane (*lt*-plane) of the wood material coincides with the *xy*-plane where the *x*-axis follows the longitudinal direction of the board and the *y*-axis follows the depth direction of the board, as shown in Fig 6(a) and (b). This means that the radial direction was assumed to be parallel with the *z*-direction of the board. Note that in-plane fiber angles observed on the narrow faces of the board, ie on surfaces that are actually parallel to the *xz*-plane are, nevertheless, regarded in the models as angles in the *lt*-plane. None of the FAM models is thus a complete 3D fiber orientation model (ie none of them provide a realistic

Table 1. Notation and definitions of IPs used for prediction of $E_{m,l,corr}$.

Notation of IP	Definition
$E_{500,IOCS,FAM1}$	$E_{500,IOCS,FAM1} = \frac{1}{5h} \sum_{x_s = x_c \pm 2.5h} E_b(x_s)\Delta x$, where $E_b(x)$, defined in Eq 10, is calculated using FAM1. x_c is the center position of the four-point bending test and x_s represents positions within the interval $\pm 2.5h$ where E_b is evaluated.
$E_{500,FE,FAM1}$	$E_{500,FE,FAM1} = E_{\bar{b},FE}(x_c, L_r = 5h)$ where $E_{\bar{b},FE}(x_c, L_r)$, defined in Eq 13, is calculated using FAM1.
$E_{500,IOCS,FAM2}$	$E_{500,IOCS,FAM2} = \frac{1}{5h} \sum_{x_s = x_c \pm 2.5h} E_b(x_s)\Delta x$ where $E_b(x)$ is calc. using FAM2.
$E_{500,FE,FAM2}$	$E_{500,FE,FAM2} = E_{\bar{b},FE}(x_c, L_r = 5h)$ where $E_{\bar{b},FE}(x_c, L_r)$ is calc. using FAM2.
$E_{500,IOCS,FAM1}$ & ρ_{corr}	The IP giving the highest R^2 to $E_{m,l,corr}$, combining $E_{500,IOCS,FAM1}$ and ρ_{corr} as predictor variables, in multiple linear regression.[a]
$E_{500,IOCS,FAM1}$ & $E_{a,corr}$	The IP giving the highest R^2 to $E_{m,l,corr}$, combining $E_{500,IOCS,FAM1}$ and $E_{a,corr}$ as predictor variables, in multiple linear regression.[a]
$E_{500,IOCS,FAM1}$ & $E_{a,corr}$ & ρ_{corr}	The IP giving the highest R^2 to $E_{m,l,corr}$, combining $E_{500,IOCS,FAM1}$, $E_{a,corr}$, and ρ_{corr} as predictor variables, in multiple linear regression.[a]

[a] By replacing $E_{500,IOCS,FAM1}$ with $E_{500,FE,FAM1}$, $E_{500,IOCS,FAM2}$, and $E_{500,FE,FAM2}$, respectively, corresponding IPs are obtained (with obvious notations and definitions).

distinction between radial and tangential material directions) but both provide representations of the angle between fiber direction and longitudinal board direction within the volume of the board. The advantage of FAM2, in comparison with FAM1, is that it takes the natural direction of knots, which is always from the pith and outwards, into account. As described, this is done by means of interpolation, in a direction from the pith and outwards, between two positions on different surfaces (to assign a fiber angle in a position of the interior of the board), as illustrated in Fig 6(b). Thus, FAM2 should give a more realistic representation of the angle between fibers and the longitudinal board direction of the inner of the board volume than what FAM1 does.

Definitions of Indicating Properties

It is now time to define all the IPs to be evaluated and compared with respect to their ability to predict local static MoE, $E_{m,l,corr}$, and bending strength, $f_{m,h}$, respectively. ρ_{corr} and $E_{a,corr}$, defined in Eqs 1 and 2, are often employed to predict grade determining properties. Thus, they are also included in the present evaluation, as both IPs in themselves and predictor variables in IPs that are based on several predictor variables and defined using linear regression.

In the "Models for calculation of local bending stiffness" and "Alternative models for fiber direction within boards" sections, in total four different versions of the grading method based on local bending stiffness determined based on fiber orientation from tracheid effect scanning were described, namely IOCS- and the FE-based methods (see "Stiffness based on integration over cross" and "Stiffness based on finite element method and simulation of bending" sections, respectively), used in combination with either FAM1 or FAM2 (see "Alternative models for fiber direction within boards" section). In Table 1, IPs based on the methods described, and intended for prediction of/comparison with the experimentally obtained $E_{m,l,corr}$, are defined. Correspondingly, in Table 2 IPs intended for prediction of $f_{m,h}$ are defined.

RESULTS AND DISCUSSION

Data Obtained from Laboratory Tests

In Table 3 mean values, standard deviations and coefficients of variation are presented for bending strength, density, local bending MoE and dynamic axial MoE of the 221 boards. Compared with results presented in other studies of properties of Douglas fir timber cultivated in France, strength, MoEs, and density of the present sample are all high. For example, the mean values of bending

Table 2. Notation and definitions of IPs used for prediction of $f_{m,h}$.

Notation of IP	Definition
$E_{90,IOCS,FAM1}$	$E_{90,IOCS,FAM1} = \frac{1}{0.090}\min_{p_1<x_p<p_2}\left(\sum_{x=x_p\pm0.045} E_b(x)\Delta x\right)$, where $E_b(x)$ is calculated using FAM1. p_1 and p_2 are the positions between which the local bending MoE is evaluated, ie $p_1 = x_c - 2.5h$ and $p_2 = x_c + 2.5h$, and x_p is any position between p_1 and p_2.
$E_{90,FE,FAM1}$	$E_{90,FE,FAM1} = \min_{p_1<x_p<p_2}\left(E_{\bar{b},FE}(x_p, L_r{=}0.090)\right)$, where $E_{\bar{b},FE}(x_c, L_r)$ is calculated using FAM1.
$E_{90,IOCS,FAM2}$	$E_{90,IOCS,FAM1} = \frac{1}{0.090}\min_{p_1<x_p<p_2}\left(\sum_{x=x_p\pm0.045} E_b(x)\Delta x\right)$, where $E_b(x)$ is calculated using FAM2.
$E_{90,FE,FAM2}$	$E_{90,FE,FAM2} = E_{\bar{b},FE}(x_c, L_r{=}0.090)$ where $E_{\bar{b},FE}(x_c, L_r)$ is calc. using FAM2.
$E_{90,IOCS,FAM1}$ & ρ_{corr}	The IP giving the highest R^2 to $f_{m,h}$, combining $E_{90,IOCS,FAM1}$ and ρ_{corr} in multiple linear regression.[a]
$E_{90,IOCS,FAM1}$ & $E_{a,corr}$	The IP giving the highest R^2 to $f_{m,h}$, combining $E_{90,IOCS,FAM1}$ and $E_{a,corr}$ in multiple linear regression.[a]
$E_{90,IOCS,FAM1}$ & $E_{a,corr}$ & ρ_{corr}	The IP giving the highest R^2 to $f_{m,h}$, combining $E_{90,IOCS,FAM1}$, $E_{a,corr}$, and ρ_{corr} in multiple linear regression.[a]

[a] By replacing $E_{90,IOCS,FAM1}$ with $E_{500,FE,FAM1}$, $E_{500,IOCS,FAM2}$, and $E_{500,FE,FAM2}$, respectively, corresponding IPs are obtained (with obvious notations and definitions).

strength, density, and dynamic MoE of the sample of 685 boards presented in Olsson et al (2018a) were only 34.7 MPa, 486 kg/m^3, and 11.0 GPa, respectively. The higher values of properties of the sample presented herein is explained by the fact that the boards are cut from larger logs than normal, about 50 cm in diameter, and wood at a larger distance to pith is stronger, stiffer, and of higher density than wood closer to pith (Kliger et al 1998). As expected, since the sample contains boards cut close to as well as far away from the pith, the coefficients of variation of the different properties are also significantly higher than those presented in Olsson et al (2018a).

Performance of Models and Indicating Properties

In Table 4 coefficients of determination and standard errors of estimate (SEE) among bending strength, density, local bending MoE, and axial dynamic MoE are presented. Coefficients of determination as well as SEEs are higher than the corresponding values presented in Olsson et al (2018a). For example, when $E_{a,corr}$ is the independent variable and $f_{m,corr}$ the dependent variable, R^2 and SEE are 0.54 and 12.6, respectively. Corresponding values reported in Olsson et al (2018a) are 0.47 and 8.57, respectively. Regarding the larger R^2, this is explained by the larger value range, ie larger coefficients of variation, of $E_{a,corr}$ and $f_{m,corr}$ for the current set of boards. Regarding the larger SEE, this is explained by the number and size of knots in outer wood boards. Some such boards are more or less free from knots in the constant bending moment zone (resulting in very high bending

Table 3. Mean value (mean), standard deviation (SD), and coefficient of variation (CoV) of mechanical properties, density, and MC.

	$f_{m,h}$ [MPa]	ρ_{corr} [kg/m^3]	$E_{m,l,corr}$ [GPa]	$E_{a,corr}$ [GPa]	u_s [%]
Mean	42.1	525	10.5	12.2	12.4
SD	18.5	48.7	3.59	2.96	0.83
CoV [%]	44	9	34	24	7

Table 4. Coefficient of determination and SEE between selected board properties.

	Independent variable →		$f_{m,corr}$	$E_{a,corr}$	$E_{m,l,corr}$	ρ_{corr}
Dependent variable	$f_{m,corr}$ [MPa]	R^2	1	0.54	0.68	0.32
		SEE	0	12.6	10.4	15.3
	$E_{a,corr}$ [GPa]	R^2	0.54	1	0.75	0.58
		SEE	2.01	0	1.49	1.93
	$E_{m,l,corr}$ [GPa]	R^2	0.68	0.75	1	0.43
		SEE	2.02	1.80	0	2.71
	ρ_{corr} [kg/m^3]	R^2	0.32	0.58	0.43	1
		SEE	40.2	31.8	36.8	0

Table 5. Coefficients of determination, R^2, between $E_{m,l,corr}$ and IPs as function (linear regression) of a single or a set of several predictor variables.

Independent variables utilized in linear regression	$E_{500,IOCS,FAM1}$ $E_{500,IOCS,FAM1}$ & ρ $E_{500,IOCS,FAM1}$ & $E_{a,corr}$ $E_{500,IOCS,FAM1}$ & $E_{a,corr}$ & ρ	$E_{500,FE,FAM1}$ $E_{500,FE,FAM1}$ & ρ $E_{500,FE,FAM1}$ & $E_{a,corr}$ $E_{500,FE,FAM1}$ & $E_{a,corr}$ & ρ	$E_{500,IOCS,FAM2}$ $E_{500,IOCS,FAM2}$ & ρ $E_{500,IOCS,FAM2}$ & $E_{a,corr}$ $E_{500,IOCS,FAM2}$ & $E_{a,corr}$ & ρ	$E_{500,FE,FAM2}$ $E_{500,FE,FAM2}$ & ρ $E_{500,FE,FAM2}$ & $E_{a,corr}$ $E_{500,FE,FAM2}$ & $E_{a,corr}$ & ρ
R^2 to $E_{m,l,corr}$	0.62	0.70	0.65	0.70
	0.72	0.79	0.75	0.80
	0.81	0.84	0.82	0.84
	0.81	0.84	0.82	0.84

strength) while others may have a single very large knot in this critical zone (resulting in very low strength). However, the difference in axial dynamic MoE may be comparatively small, which results in larger prediction errors.

In Table 5, coefficient of determination among local bending MoE, $E_{m,l,corr}$, and IPs is presented, the latter based on a single or a set of independent variables as described and defined in Table 1. Thus each column in this table represents one of the four different model combinations (IOCS or FEM in combination with FAM1 or FAM2) for calculation of local bending MoE over a span of $5h$ (500 mm). Comparing first the performance of the single independent variables $E_{500,IOCS,FAM1}$, $E_{500,FE,FAM1}$, $E_{500,IOCS,FAM2}$, and $E_{500,FE,FAM2}$, it is shown, as expected, that the FE model enables better prediction of local MoE than what the simpler IOCS model does, with R^2 of 0.70 using the FE model (FAM1 or FAM2 give the same R^2) and 0.62 and 0.65 using the IOCS model (in combination with FAM1 and FAM2, respectively). Comparing next the increase of coefficients of determination when adding ρ or $E_{a,corr}$ as additional independent variables to $E_{m,l,corr}$, any of them contribute to raise the coefficient of determination. $E_{a,corr}$ gives larger improvement than what ρ does. Combined use of $E_{a,corr}$ and $E_{500,FE,FAM1}$ (or $E_{500,FE,FAM2}$) gives an R^2 to $E_{m,l,corr}$ as high as 0.84. Adding ρ as a third independent variable does not give further improvement.

In Table 6 coefficients of determination between $f_{m,corr}$ and IPs are presented. Here, the independent variables based on the four models (IOCS or FEM in combination with FAM1 or FAM2) represent local bending MoE over spans of only 90 mm, rather than over 500 mm as is the case for the predictor variables used Table 5. Comparison of performance of the four alternative models, represented by $E_{90,IOCS,FAM1}$, $E_{90,FE,FAM1}$, $E_{90,IOCS,FAM2}$, and $E_{90,FE,FAM2}$, respectively, to predict $f_{m,corr}$ leads to similar conclusions as regarding prediction of $E_{m,l,corr}$ in the sense that the FE model gives more accurate prediction of $f_{m,corr}$ than what the IOCS model does, even though the improvement of using the FE model is not quite as large as for prediction of $E_{m,l,corr}$. However, results shown in Table 6 indicate that FAM2 give better prediction of $f_{m,corr}$ than what FAM1 does and, consequently, the highest coefficient of determination

Table 6. Coefficients of determination R^2 between $f_{m,corr}$ and IPs as function (linear regression) of a single or a set of several predictor variables.

Independent variables utilized in linear regression	$E_{90,IOCS,FAM1}$ $E_{90,IOCS,FAM1}$ & ρ $E_{90,IOCS,FAM1}$ & $E_{a,corr}$ $E_{90,IOCS,FAM1}$ & $E_{a,corr}$ & ρ $E_{a,corr}$ & ρ	$E_{90,FE,FAM1}$ $E_{90,FE,FAM1}$ & ρ $E_{90,FE,FAM1}$ & $E_{a,corr}$ $E_{90,FE,FAM1}$ & $E_{a,corr}$ & ρ	$E_{90,IOCS,FAM2}$ $E_{90,IOCS,FAM2}$ & ρ $E_{90,IOCS,FAM2}$ & $E_{a,corr}$ $E_{90,IOCS,FAM2}$ & $E_{a,corr}$ & ρ	$E_{90,FE,FAM2}$ $E_{90,FE,FAM2}$ & ρ $E_{90,FE,FAM2}$ & $E_{a,corr}$ $E_{90,FE,FAM2}$ & $E_{a,corr}$ & ρ
R^2 to $f_{m,corr}$	0.61	0.65	0.64	0.68
	0.70	0.72	0.73	0.75
	0.70	0.72	0.72	0.74
	0.71	0.73	0.74	0.76
	0.54	—	—	—

using a single independent variable is obtained for $E_{90,FE,FAM2}$, for which $R^2 = 0.68$. Adding ρ or $E_{a,corr}$ as a second independent variable to predict $f_{m,corr}$ means considerable improvement. It is interesting to note that ρ gave at least as large improvement to the coefficient of determination as what $E_{a,corr}$ did. However, for other samples of Douglas fir and Norway spruce (Olsson et al 2018a) $f_{m,corr}$ was more accurately predicted using [$E_{90,IOCS,FAM1}$ & $E_{a,corr}$] than using [$E_{90,IOCS,FAM1}$ & ρ].

In Fig 7(a) graphical illustration is given of some of the results presented in Table 6. In Fig 7(a), the scatter plot and linear regression line between $f_{m,corr}$ and [$E_{90,IOCS,FAM1}$ & $E_{a,corr}$ & ρ] with $R^2 = 0.71$ and SEE = 10.0 MPa is shown. This IP is similar to the original one first suggested by Olsson et al (2013) which was also based on IOCS and FAM1 (although in the present study, only the part of the board of length $5h$, centered between the point loads in the destructive test is actually considered. See the definition given in Table 1). In Fig 7(b), the scatter plot between $f_{m,corr}$ and [$E_{90,FE,FAM2}$ & $E_{a,corr}$ & ρ] with $R^2 = 0.76$ and SEE = 9.2 MPa is shown, and in Fig 7(c) the scatter plot between $f_{m,corr}$ and $E_{a,corr}$ with $R^2 = 0.54$ and SEE = 12.6 MPa. The histogram in Fig 7(d) shows the errors of estimated modulus

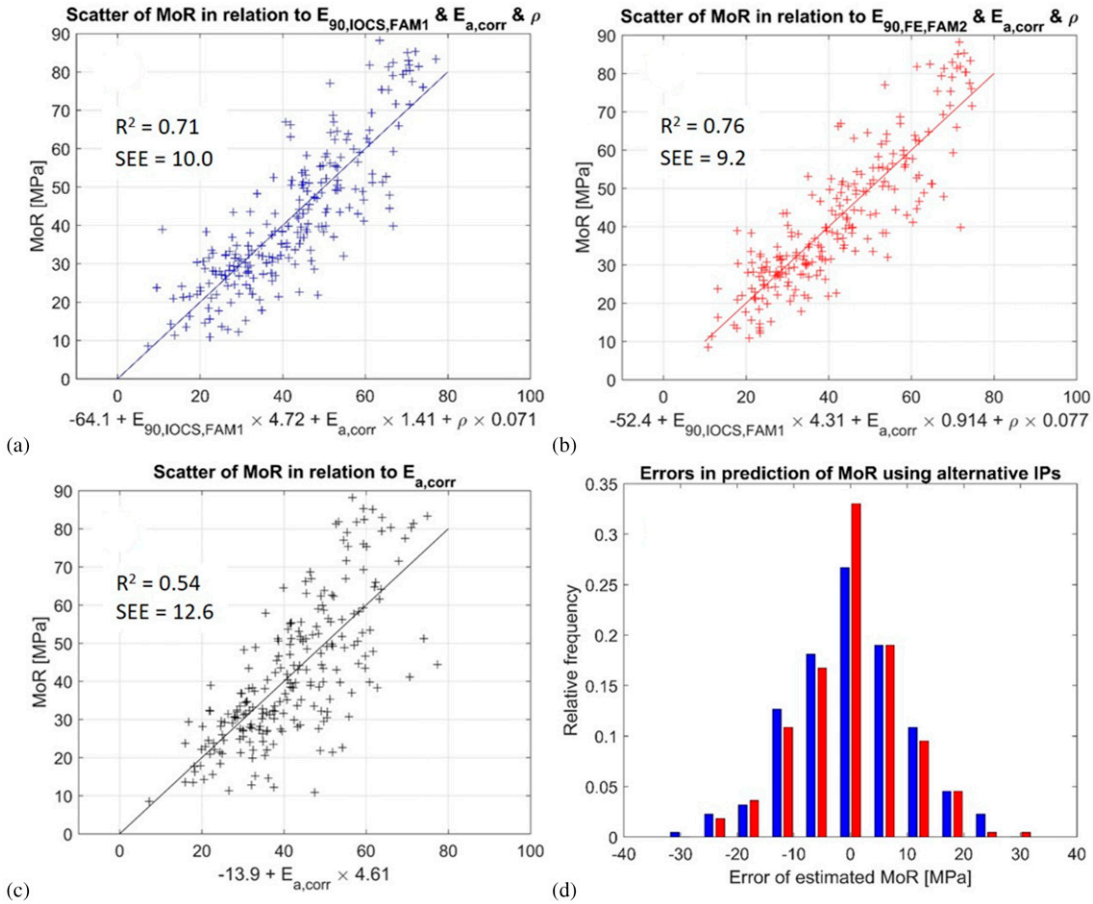

Figure 7. Selected results of relationships between IPs and MoR ($f_{m,corr}$); (a-c) scatter plots and results of linear regression of [$E_{90,IOCS,FAM1}$ & $E_{a,corr}$ & ρ], [$E_{90,FE,FAM2}$ & $E_{a,corr}$ & ρ], and $E_{a,corr}$, respectively, to MoR and (d) histogram of errors of estimated MoR using as IP [$E_{90,IOCS,FAM1}$ & $E_{a,corr}$ & ρ] (blue bars) and [$E_{90,FE,FAM2}$ & $E_{a,corr}$ & ρ] (red bars).

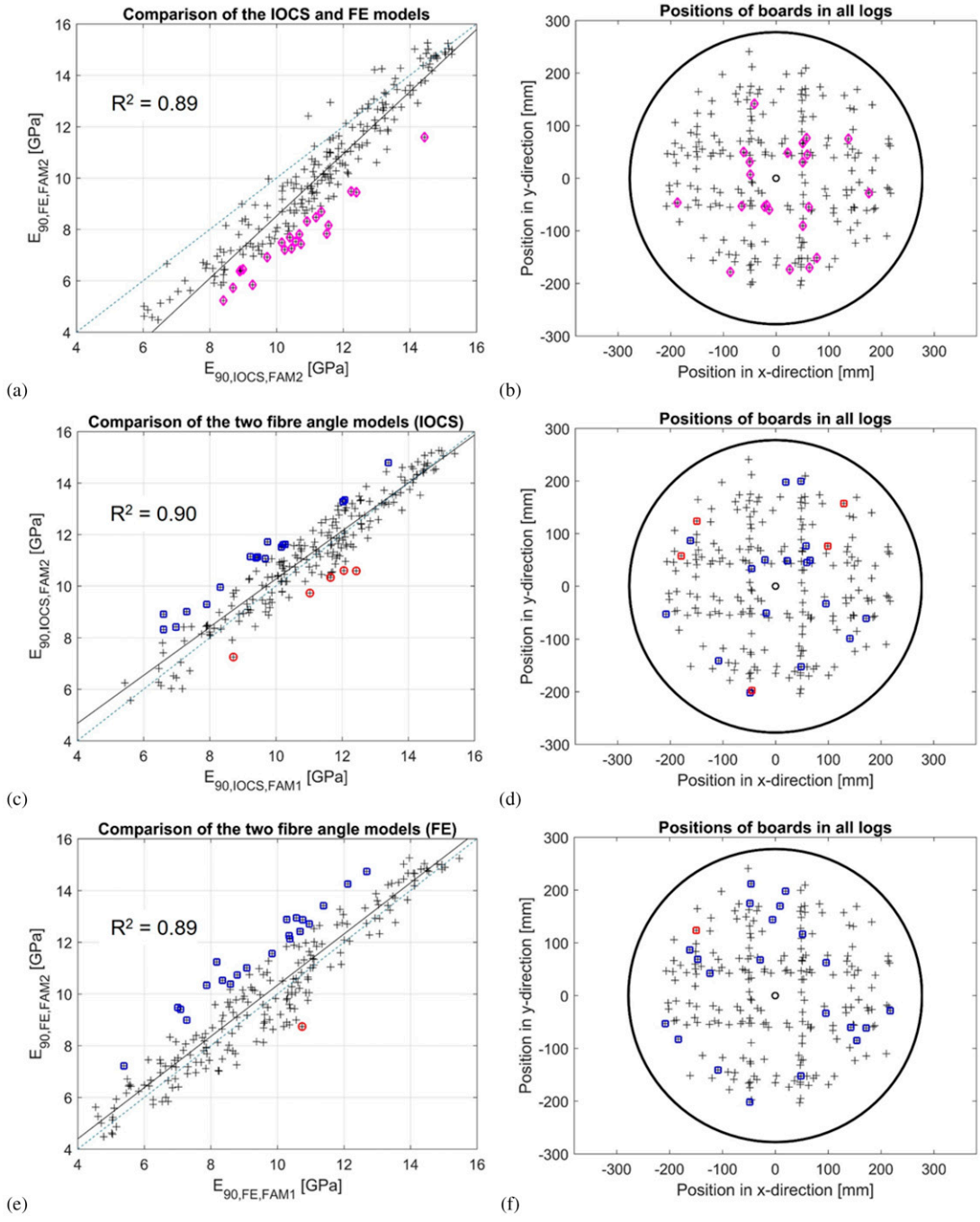

Figure 8. Relationships between calculated local bending stiffness using the IOCS and the FE models, and using FAM1 and FAM2, along with positions of highlighted boards in relation to pith of the log; (a and b) $E_{90,FE,FAM2}$ vs $E_{90,IOCS,FAM2}$; (c and d) $E_{90,IOCS,FAM2}$ vs $E_{90,IOCS,FAM1}$; (e and f) $E_{90,FE,FAM2}$ vs $E_{90,FE,FAM1}$.

of rupture (MoR) using [$E_{90,IOCS,FAM1}$ & $E_{a,corr}$ & ρ] (bars in blue) and [$E_{90,FE,FAM2}$ & $E_{a,corr}$ & ρ] (bars in red), where the latter shows a noticeable improvement compared with the former.

Some further analysis of the differences between IOCS and FE models, and between FAM1 and FAM2 follows. In Fig 8(a), a scatter plot between the predictors $E_{90,IOCS,FAM2}$ and $E_{90,FE,FAM2}$ is shown. The 10% of the boards with largest values of $|E_{90,IOCS,FAM2}-E_{90,FE,FAM2}|$ are highlighted (magenta diamonds). The solid line through the scatter plot is the linear regression line and the dashed line is given by $y = x$. As expected, the FE model (represented by $E_{90,FE,FAM2}$) gives, for most the boards, a lower calculated bending stiffness than what the IOCS model (represented by $E_{90,IOCS,FAM2}$) does. This is because the IOCS model tends to overestimate the bending stiffness as explained in the "Stiffness based on integration over cross section" section. The very idea of replacing IOCS with FE was to resolve this. For a few boards, however, especially boards with high calculated bending stiffness, the FE model gives slightly higher stiffness than what the IOCS model does. This is because the FE mesh and the linear elements used give a somewhat too high bending stiffness. Thus, the conclusion drawn from an introductory convergence study (see "Stiffness based on finite element method and simulation of bending" section and Hu et al 2018) was not quite accurate. With a finer element mesh and/or use of higher order elements, the FE model would not give higher stiffness than the IOCS model for any of the boards. In Fig 8(b) the position of the center of each board's end cross section, in relation to the pith of the log from which it is cut, is indicated. Just as in Fig 8(a), the boards with largest values of $|E_{90,IOCS,FAM2}-E_{90,FE,FAM2}|$ are highlighted (magenta diamonds) and it can be seen in Fig 8(b) that most of these boards are located closer to pith than the average board of the sample. Closer to pith it is more common 1) that several knots are located close to each other and therefore may have an influence on the bending stiffness of the 90 mm long section along the board for which the bending stiffness is calculated, and 2) that knots are not directed in a 90 degree angle to the direction of the board, since the angle between the direction of a certain branch/knot and the direction of the tree is smaller for the younger tree than for the older tree. For these reasons, the FE model was expected to result in lower bending stiffness particularly for boards cut close to the pith, and this is precisely what is indicated by the results shown in Fig 8(a) and (b). For a sample of boards cut from smaller logs it is likely that the difference of results, comparing $E_{90,IOCS,FAM2}$ with $E_{90,FE,FAM2}$, would be larger, rather than smaller, since then a higher proportion of the boards would be located close to the pith.

In Fig 8(c) and (e), scatter plots between $E_{90,IOCS,FAM1}$ and $E_{90,IOCS,FAM2}$, and between $E_{90,FE,FAM1}$ and $E_{90,FE,FAM2}$, are shown. Thus, both plots represent comparisons between FAM1 and FAM2. The 10% of the boards with largest difference of calculated bending stiffness using FAM1 and FAM2, ie largest values of $|E_{90,IOCS,FAM1}-E_{90,IOCS,FAM2}|$ and $|E_{90,FE,FAM1}-E_{90,FE,FAM2}|$ are highlighted (blue squares when FAM2 gives higher stiffness and red circles when FAM1 gives higher stiffness). For most of the highlighted boards (boards with the largest difference in stiffness) FAM2 gives the higher stiffness. In Fig 8(d) and (f), the positions of the boards in relation to pith of the log are shown. No very clear pattern is, however, identified regarding the position of the cross sections of highlighted boards in relation to the pith.

CONCLUSIONS AND FURTHER WORK

Two different potential improvements of a method to predict bending strength of sawn timber were evaluated herein using a relatively large sample of Douglas fir boards. The improvements consists of 1) the use a 3D FE model, rather than a model based on simple IOCSs, to calculate the local bending MoE over weak section of length 90 mm in longitudinal board direction and 2) a more realistic model of the local angle between wood fibers and longitudinal board direction in the interior of boards, taking location of pith and directions of knots into account.

Results show that the use of the 3D FE model, rather than the simpler IOCS model, allows for more accurate prediction of bending stiffness. For prediction of the local bending MoE over five times the larger board dimension, $E_{m,l,corr}$, the coefficient of determination increased from $R^2 = 0.62$ to $R^2 = 0.70$ when using data from fiber orientation measurements alone, and from $R^2 = 0.81$ to $R^2 = 0.84$ when based on data of fiber orientation in combination with data of board resonance frequency and density. For prediction of bending strength, $f_{m,corr}$, the coefficient of determination increased from $R^2 = 0.61$ to $R^2 = 0.65$ when using data from fiber orientation measurements alone, and from $R^2 = 0.71$ to $R^2 = 0.73$ when based on data of fiber orientation, resonance frequency and density. Thus, the results indicate that the use of a 3D FE model, rather than simple IOCS, for calculation of local bending MoE as IP to bending strength gives an improvement. The employed FE model is quite simple and with suitable implementation in computer code, it would be possible to use it for grading in production speed.

The use of the more advanced model for fiber angles of the interior of the board did not contribute significantly to increased accuracy in prediction of $E_{m,l,corr}$. When using data from fiber orientation in combination with data of resonance frequency and density, about the same accuracy was obtained no matter if FAM1 or FAM2 was used ($R^2 = 0.81$ and 0.82, respectively using IOCS, and $R^2 = 0.84$ using FE). For prediction of $f_{m,corr}$, however, the coefficient of determination increased from $R^2 = 0.61$ to $R^2 = 0.64$ when using data from fiber orientation measurements alone, and from $R^2 = 0.71$ to $R^2 = 0.74$ (using IOCS) and from $R^2 = 0.73$ to $R^2 = 0.76$ (using FE) when based on data of fiber orientation, resonance frequency and density. It should be noted, however, that application of the improved fiber angle model requires knowledge of approximate location of pith for each board assessed. In this study such knowledge was obtained manually, on one end of the boards. However, it has recently been shown that location of pith can be determined automatically, in very high speed and with high resolution along the board (Habite et al 2022).

Combining the 3D FE model with the improved fiber angle model (FAM2) was quite successful and gave a coefficient of determination to $f_{m,corr}$ as high as $R^2 = 0.76$. Thus, altogether, an increase in coefficient of determination of about 0.05 was achieved. This represents a considerable improvement of the original IP and grading method first proposed by Olsson et al (2013).

The basic idea behind the machine strength grading method discussed herein is to calculate a local bending MoE over a short length of only about 90 mm, and that this correlates strongly to bending strength. The work presented herein contributes to more accurate determination of such local bending MoE. The herein suggested model for fiber angle in the interior of the board still represents a considerable simplification of the true 3D fiber orientation and it is possible that further improvements of the fiber orientation model may contribute to further increase of grading accuracy using the evaluated method. However, the accuracy obtained herein ($R^2 = 0.76$ between IP and $f_{m,corr}$) may be close to what can be achieved using this concept.

Further development toward more accurate grading than what has been achieved herein may require either some new, complementary predictor variable, one that is not strongly correlated with those employed herein, or a model of the board by which strength can be calculated in a more direct way, ie not only via calculation of local bending MoE. It is, however, likely that such calculation of strength would require a model of the fiber orientation around knots that is more accurate than the one employed herein. Thus, development of such models is yet another subject for further research and development in this field.

ACKNOWLEDGMENTS

This research was made possible through financial support of the Bourgogne Franche-Comté regional council and the French National Research Agency (ANR) in the framework of the TreeTrace project, ANR-17-CE10-0016.

REFERENCES

Bacher M (2008) Comparison of different machine strength grading principles. *in* Proceedings, 2nd Conference

COST Action E53—Quality Control for Wood and Wood Products, October 29-30, Delft, the Netherlands.

Briggert A, Hu M, Olsson A, Oscarsson J (2018) Tracheid effect scanning and evaluation of in-plane and out-of-plane fiber direction in Norway spruce using. Wood Fiber Sci 50(4):411-429.

Briggert A, Olsson A, Oscarsson J (2020) Prediction of tensile strength of sawn timber: Definitions and performance of indicating properties based on surface laser scanning and dynamic excitation. Mater Struct 53(54):1-20.

Daval V, Pot G, Belkacemi M, Meriaudeau F, Collet R (2015) Automatic measurement of wood fiber orientation and knot detection using an optical system based on heating conduction. Opt Express 23:33529-33539.

EN 384 (2016). Structural timber—Determination of characteristics values of mechanical properties and density. European Committee for Standardization.

EN 408 (2010) + A1 (2012). Timber structures—Structural timber and glued laminated timber—Determination of some physical and mechanical properties. European Committee for Standardization.

EN 14081-2 (2018). Timber structures—Strength graded structural timber with rectangular cross section—Part 2: Machine grading; additional requirements for type testing. European Committee for Standardization.

Foley C (2003) Modeling the effects of knots in structural timber. Doctoral thesis, Report TVBK-1027, Lund Inst of Technol, Lund, Sweden.

Habite T, Abdeljaber O, Olsson A (2021) Automatic detection of annual rings and pith location along Norway spruce timber boards using conditional adversarial networks. Wood Sci Technol 55:461-488.

Habite T, Abdeljaber O, Olsson A. (2022) Determination of pith location along Norway spruce timber boards using one dimensional convolutional neural networks trained on virtual timber boards. Constr Build Mater 329:127129. https://doi-org.proxy.lnu.se/10.1016/j.conbuildmat.2022.127129

Habite T, Abdeljaber O, Oscarsson J (2020) Automatic detection of pith location along Norway spruce timber boards on the basis of optical scanning. Eur J Wood Wood Prod 78:1061-1074. https://doi-org.proxy.lnu.se/10.1007/s00107-020-01558-1

Hanhijärvi A, Ranta-Maunus A (2008) Development of strength grading of timber using combined measurement techniques. Report of the Combigrade-Project—Phase 2. VTT Publications 686.

Hu M, Olsson A, Johansson M, Oscarsson J (2018) Modelling local bending stiffness based on fiber orientation in sawn timber. Eur J Wood Wood Prod 76(6): 1605-1621.

Jenkel C, Kaliske M (2018) Simulation of failure in timber with structural inhomogeneities using an automated FE analysis. Comput Struct 207:19-36. https://doi-org.proxy.lnu.se/10.1016/j.compstruc.2017.11.016

Kandler G, Lukacevic M, Füssl J (2016) An algorithm for the geometric reconstruction of knots within timber boards based on fiber angle measurements. Constr Build Mater 124:945-960. https://doi-org.proxy.lnu.se/10.1016/j.conbuildmat.2016.08.001

Kliger R, Perstorper M, Johansson G (1998) Bending properties of Norway spruce timber. Comparison between fast- and slow-grown stands and influence of radial position of sawn timber. Ann Sci 55(3):349-358. https://hal.archives-ouvertes.fr/hal-00883206

Lukacevic M, Füssl J, Eberhardsteiner J (2015) Discussion of common and new indicating properties for the strength grading of wooden boards. Wood Sci Technol 49(3):551-576. https://doi-org.proxy.lnu.se/10.1007/s00226-015-0712-1

Lukacevic M, Kandler G, Hu M, Olsson A, Füssl J (2019) A 3D model for knots and related fiber deviations in sawn timber for prediction of mechanical properties of boards. Mater Des 166:1-18. https://doi-org.proxy.lnu.se/10.1016/j.matdes.2019.107617

Matthews P, Beech B (1976) Method and apparatus for detecting timber defects. U.S. Patent 3976384.

Nocetti M, Bacher M, Brunetti M, Crivellaro A, van de Kuilen JWG (2010) Machine grading of Italian structural timber: Preliminary results on different wood species. *in* Proceedings, 11th World Conference on Timber Engineering, June 20-24, Riva del Garda, Italy.

Olsson A, Oscarsson J (2017) Strength grading on the basis of high resolution laser scanning and dynamic excitation: A full scale investigation of performance. Eur J Wood Wood Prod 75:17-31. https://doi-org.proxy.lnu.se/10.1007/s00107-016-1102-6

Olsson A, Oscarsson J, Serrano E, Källsner B, Johansson M, Enquist B (2013) Prediction of timber bending strength and in-member cross-sectional stiffness variation on the basis of local wood fiber orientation. Eur J Wood Wood Prod 71(3):319-333. https://doi-org.proxy.lnu.se/10.1007/s00107-013-0684-5

Olsson A, Pot G, Viguier J, Faydi Y, Oscarsson J (2018a) Performance of strength grading methods based on fiber orientation and axial resonance frequency applied to Norway spruce (*Picea abies* L.), Douglas fir (*Pseudotsuga menziesii* (Mirb.) Franco) and European oak (*Quercus petraea* (Matt.) Liebl./*Quercus robur* L.). Ann Sci 75(102):1-18. https://doi-org.proxy.lnu.se/10.1007/s13595-018-0781-z

Olsson A, Serrano E, Oscarsson J, Enquist B, Johansson M, Källsner B (2018b) Method and device for evaluating a wooden board. US 9,863,929 B2.

Oscarsson J (2014) Strength grading of structural timber and EWP laminations of Norway spruce—Development potentials and industrial applications, Report no. 170/2014, Linnaeus University, Växjö, Sweden.

Sarnaghi AK, van de Kuilen JWG (2019) An advanced virtual grading method for wood based on surface information of knots. Wood Sci Technol 53:535-557. https://doi-org.proxy.lnu.se/10.1007/s00226-019-01089-w

Soest J, Matthews P, Wilson B (1993) A simple optical scanner for grain defects. *in* Proceeding, 5th Int Conference Scanning Technologies & Process Control for the Wood Prod Industry, October 25-27, Atlanta, GA.

Viguier J, Bourreau D, Bocquet JF, Pot G, Bléron L, Lanvin JD (2017) Modelling mechanical properties of spruce and Douglas fir timber by means of X-ray and grain angle measurements for strength grading purpose. Eur J Wood Wood Prod 75(4):527-541.

Wright S, Dahlen J, Montes C, Eberhart T (2019) Quantifying knots by image analysis and modeling their effects on the mechanical properties of loblolly pine lumber. Eur J Wood Wood Prod 77:903-917. https://doi-org.proxy.lnu.se/10.1007/s00107-019-01441-8